Evaporative Crystallization of Spirals
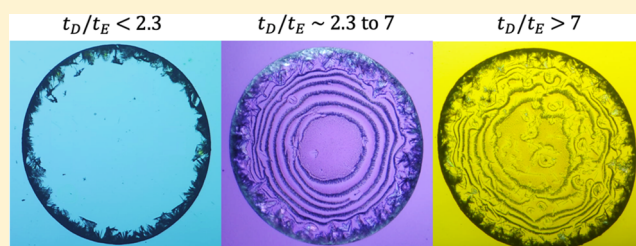
Samantha A. McBride,[†] Susmita Dash,[‡] Sami Khan,[†] and Kripa K. Varanasi*,[†]

[†]Department of Mechanical Engineering, Massachusetts Institute of Technology, 77 Massachusetts Avenue, Cambridge, Massachusetts 02139, United States

[‡]Department of Mechanical Engineering, Indian Institute of Science, CV Raman Road, Bengaluru 560012, India

Ⓢ *Supporting Information*

ABSTRACT: Spiral motifs are pervasive in nature, art, and technology due to their functional property of providing compact length. Nature is particularly adept at spiral patterning, and yet, the spirals observed in seashells, hurricanes, rams' horns, flower petals, etc. all evolve via disparate physical mechanisms. Here, we present a mechanism for the self-guided formation of spirals from evaporating saline drops via a coupling of crystallization and contact line dynamics. These patterns are in contrast to commonly observed patterns from evaporation of colloidal drops, which are discrete (rings, concentric rings) or continuous (clumps, uniform deposits) depending on the particle shape, contact line dynamics, and evaporation rate. Unlike the typical process of drop evaporation where the contact line moves radially inward, here, a thin film pinned by a ring of crystals ruptures radially outward. This motion is accompanied by a nonuniform pinning of the contact line due to crystallization, which generates a continuous propagation of pinning and depinning events to form a spiral. By comparing the relevant timescales of evaporation and diffusion, we show that a single dimensionless number can predict the occurrence of these patterns. These insights on self-guided crystallization of spirals could be used to create compact length templates.

$t_D/t_E < 2.3$ $t_D/t_E \sim 2.3$ to 7 $t_D/t_E > 7$

INTRODUCTION

Spirals have long captivated the human imagination and are a recurrent theme in art ranging from prehistoric to modern. Nature, too, is apparently infatuated with spirals as they appear in hundreds of naturally occurring phenomena:[1] the arrangement of flower seeds and petals, galaxies, seashells, the α-helix of DNA, hurricanes, the cochlea of the inner ear, convection patterns,[2] and more.[1] Despite the universality, each of these examples form via disparate physical mechanisms. Here, we present a mechanism for the unguided assembly of spirals from evaporating saline drops via a coupling of crystallization and contact line dynamics.

Evaporative deposition of particles from drops is a surprisingly useful and simple tool for microscale self-assembly. In most reports, colloidal particles within evaporating drops assemble into three common patterns: rings,[3] concentric rings,[4] and filled deposits.[5] The preference of a system for one deposit pattern over another is dictated by the particle shape/size,[5,6] substrate wettability,[7] temperature, etc. and can be predicted by a balance between particle–substrate interactions, convection, and evaporation rate.[8] Evaporative deposition has found application in inkjet printing, size separations,[6] colloidal crystals,[9] diagnostics,[10] and more.[11]

Evaporation of a saline drop also results in deposition patterns. During evaporation, nonvolatile solutes become concentrated beyond their solubility limit and precipitate as crystals. Crystallization from drops has additional complexity compared to the deposition of colloids from drops due to the interdependence of the flow and emerging crystals.[12] Many

crystals will preferentially nucleate at either the air/water interface, water/solid interface, or the three-phase contact line due to lowered energy barriers for nucleation,[13−15] and thus will form ring deposits even on hydrophobic or superhydrophobic surfaces.[12,15] In addition, because crystals grow into specific morphologies (the crystal habit), deposits may be three-dimensional[16,17] depending on the crystal chemistry and wettability.[12,15]

The behavior of an evaporating drop is characterized by the dynamic contact angles, and particularly by the receding contact angle (i.e., the angle at which the drop contact line begins to move inward).[18,19] In the present work, we evaporate solutions of calcium sulfate on substrates of extreme contact angle hysteresis ($\theta_A \sim 80-110°$, $\theta_R \sim 5-40°$, $\Delta\theta > 45°$, where θ_A is the substrate advancing angle, θ_R is the substrate receding angle, and $\Delta\theta$ is the contact angle hysteresis: $\Delta\theta = \theta_A - \theta_R$).[20] Previous work has demonstrated that calcium sulfate crystals will form three-dimensional structures on hydrophobic surfaces and flat, two-dimensional patterns on hydrophilic substrates.[12] Thus, we predict that the large contact angle hysteresis of these substrates will enable a dual behavior with both two-dimensional and three-dimensional structures. As we will show, the occurrence of a two-dimensional deposit within a three-dimensional ring structure is dependent on the rate of crystallization at the moving contact line.
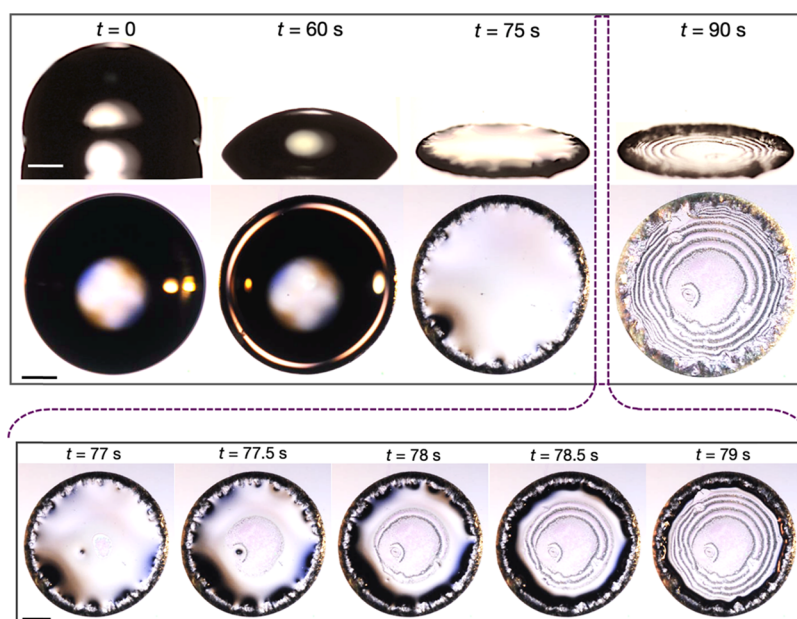
Figure 1. Evaporation of a drop on a high advancing, low receding contact angle substrate ($\theta_A = 98°$, $\theta_R = 18°$, $T = 70$ °C). The first row shows a side view, the second row shows a top-down view of drop evaporation, and the last row shows a top-down view of the thin-film rupture and contact line motion that leads to pattern formation on the drop interior. The scale bar is 0.5 mm.
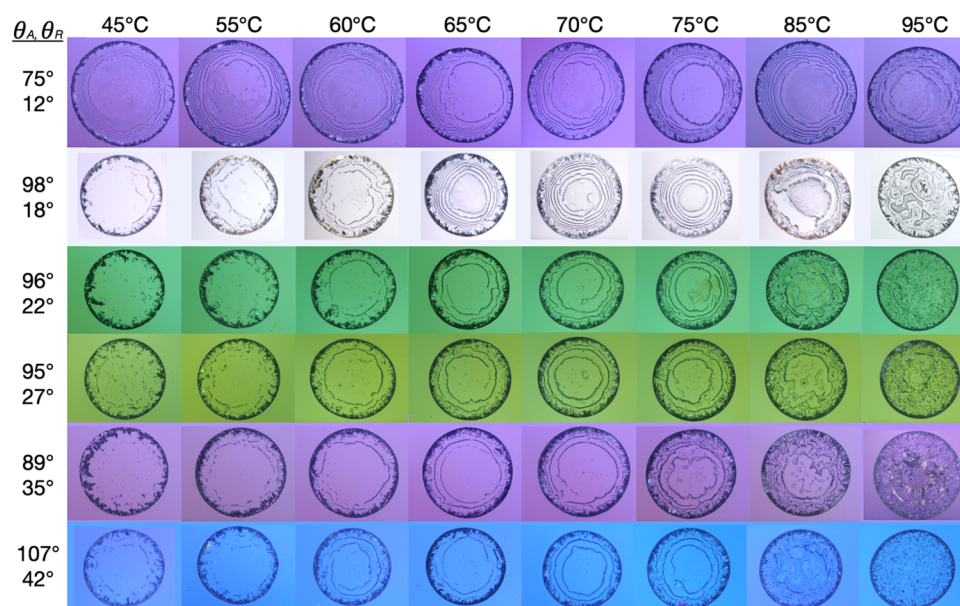

Figure 2. Selection of patterns formed on different substrates and temperatures. Different substrate colors are due to thickness and chemistry of the sputtered surface coating (see SI for characterization). The length scale is the same for all images and is 2.8 mm wide.

■ RESULTS AND DISCUSSION

Our experiments consist of evaporating 5 μL water drops containing calcium sulfate salt dissolved to its solubility concentration on heated (between 45 and 95 °C) substrates with high contact angle hysteresis ($\Delta\theta > 45°$; see Methods). Calcium sulfate solution was prepared at room temperature, but the saturation concentration remains relatively constant with temperature (2.4 g/L at 20 °C and ~2.1 g/L 100 °C for calcium sulfate dihydrate (gypsum)—the dominant polymorph at these conditions). Because of the low receding contact angle, drops remain pinned to the substrate throughout evaporation and maintain a constant contact radius. As evaporation proceeds, gypsum crystals form in a three-

dimensional ring at the contact line, an expected and previously observed result (Figure 1).[12,15] However, as the drop gets close to complete evaporation, the geometry deviates strongly from a spherical cap,[21] and a thin film pinned by the exterior crystal ring develops. This film ruptures at the center of the drop and propagates radially outward toward the ring of crystals in a mode that falls into neither of the classic modes of drop evaporation (constant contact angle and constant contact radius).[22] The ruptured film is pinned by salt crystals that form at the newly formed contact line near the drop center, leaving behind a record of the contact line movement. This results in individual gypsum needles that align into a spiral, as shown in Figure 1. In contrast, spiral patterning does not occur for a

drop containing latex nanoparticles under the same experimental conditions, suggesting that this patterning is unique to crystallizing solutes (see the Supporting Information (SI) for results using a particle-laden drop).[8,23,24]

The unusual geometry of the system during the final stages of evaporations leads to contact line motion that leaves a record in the form of crystals, as shown in the last row of Figure 1. The time required for complete evaporation after initial rupture is different from the timescales usually associated with drop evaporation. It also deviates from timescales associated with inertially driven rupture.[25] Solving a mass balance equation for the unusual geometry of the system allows for derivation of the timescale shown in the last row of Figure 1 as $t_b = h_C R_o / 3\pi J_o$ (where h_c is the height of the outer crystalline ring, R_o is the deposit radius, and J_o is the evaporative flux in m^2/s; see SI for derivation and experimental data).

An experimental matrix containing six substrates and eight substrate temperatures was used to study this phenomenon (Figure 2). At low temperatures (below ~60 °C), evaporation is slow and salt crystallizes at the contact line, forming a ring shape with a radius identical to that of the initially deposited drop. Increasing substrate temperature beyond 85 °C causes evaporation to occur rapidly, resulting in disordered, amorphous crystalline deposits that fill the center of the ring. Patterning only occurs at intermediate temperatures when some amount of the salt precipitates in the center to form regular patterns that mirror the movement of the contact line. As a general trend, we observe that lower substrate receding contact angles (θ_R) result in tighter winding of the spirals or rings and that spirals are more likely to form on these substrates (see SI, Table S7).

Both spiral and concentric ring patterns emerge from these experiments depending on the uniformity of the pinning of the contact line. Concentric rings form when the contact line pins and depins uniformly, and spirals emerge when the contact line pins nonuniformly in the azimuthal direction (i.e., when one side pins faster than the others), as shown in Figure 3. The formation of concentric rings has been well quantified for
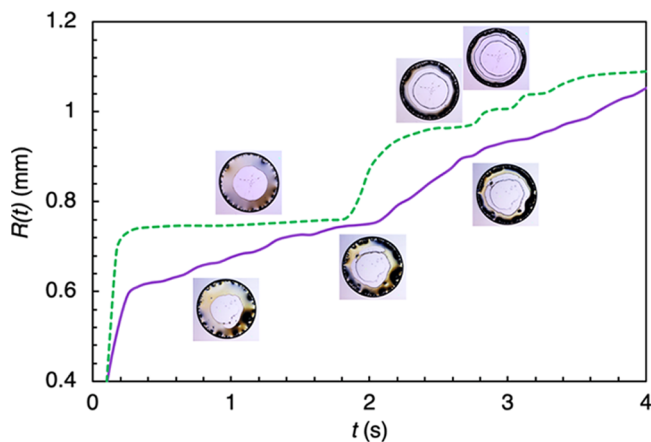
colloidal deposits and is due to the "stick-slip" phenomenon where an energy barrier periodically prevents contact line movement.[26−28] The volume loss for an evaporating drop with a pinned contact line manifests as a steady decrease in contact angle. When this contact angle reaches the receding angle for the substrate (this angle will be significantly lowered from that of pure water due to crystallization at the contact line), the drop will "slip" in a sudden decrease in contact radius and then continue to evaporate in constant contact radius mode at the new radius. Spiral patterns form from a similar behavior, except that the pinning/depinning is not global across the contact line. Instead, one portion of the contact line is constantly depinning while another portion pins at a different location so that the radius increases smoothly with time. Spirals may be more likely to form on substrates with lower receding contact angles due to the resistance of the system to depinning events.

The observation of spirals from drops is unusual. However, this phenomenon is not entirely unique to the high hysteresis surfaces used in the present study. Previous investigations have observed equidistant spiral deposition of fullerene crystals on hydrophilic substrates when used in conjunction with a glass bead placed at the center of the drop.[29−31] In these studies, the moving interface retracted from the outside of the drop inward toward the glass bead, leaving behind Archimedean spirals (in which the spirals become more tightly wound as the interface approaches the glass bead). Different spiral windings are found as a function of concentration[29,31] and temperature.[30] Comparing details of that investigation to the present reveals that both involve crystallization at a contact line moving toward a three-dimensional structure, suggesting that the unusual geometry of our system with the three-dimensional outer crystalline ring allows for formation of the two-dimensional crystalline patterns on the interior. To quantify this effect, we develop a model of the geometry of the system during the final phases of evaporation, as shown in Figure 4a (side view) and Figure 4b (top-down view).

When spirals form in these experiments, the emergent patterns are well described by Fermat's spiral equation. Fermat's spiral is a subclass of Archimedean spirals with a dependence of radius r on the square root of the polar angle $\varnothing$ ($r = a\sqrt{\varnothing}$, where a is a proportionality constant).[32] Fermat's spiral has the special property of having zero curvature at the origin and a decreasing distance between subsequent arcs. Figure 5a shows an SEM image of a characteristic spiral shape with an overlay of the relevant solution to Fermat's spiral equation. Inspection of Figure 2 demonstrates that lowered substrate receding angles decrease the distance between subsequent arcs, which corresponds to a lowered value of the proportionality parameter "a", which describes the relative distance between concentric arcs of the spiral. We expect that this parameter will be heavily dependent on the relative rates of pinning and depinning of the moving contact line. When the pinning rate is low, the interface can significantly recede before repinning, and the value of a will be high. If the pinning rate is higher than the depinning rate, the contact line will not recede significantly before another row of crystals begins to form, and a will be low.

The dependence of the spiral shape on the stick-slip motion of the contact line can be quantified following a mass balance argument,[28] where the distance between concentric rings is estimated in the limit where the volume lost to evaporation is negligible during the short timescale of a stick-slip event. We consider a triangle-shaped wedge of fluid (see the inset of
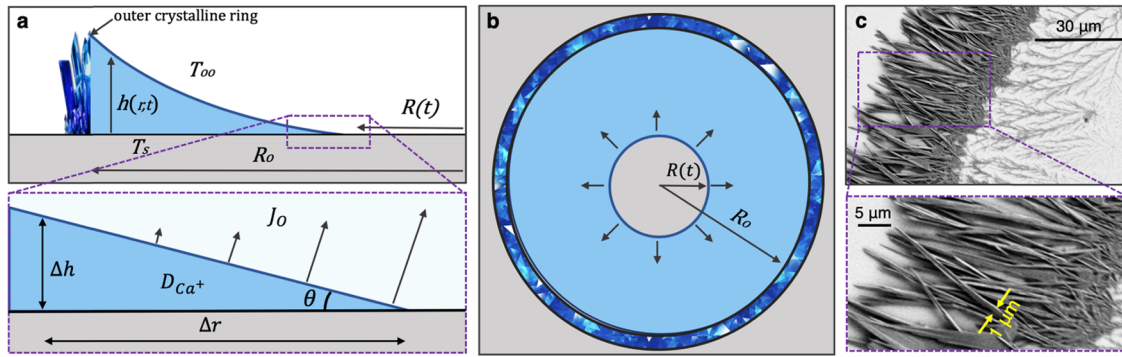

Figure 3. Position of the moving contact line after drop rupture (where $R(t) = 0$ indicates the drop center) as a function of time for a concentric ring (green dashed line) and for a spiral (purple continuous line). The concentric ring demonstrates a terraced dependence, where the contact line sticks at the position of the ring over a period of time, while the spiral contact line demonstrates a smoother dependence.

Figure 4. (a) Schematic of the geometry of the drop during thin-film evaporation, where $R(t)$ is the position of the moving contact line, R_o is the radius between the center of the drop and the outer crystal ring, $h(r, t)$ is the height profile of the liquid, and J_o is the evaporative flux. At the moving contact line $R(t)$, the evaporative flux is at a maximum and the height profile can be approximated as a triangular wedge. (b) Schematic showing drop geometry from a top view. (c) Scanning electron microscopy (SEM) image showing the size of the crystalline needles, where the width of the needles serves as an estimate for the film thickness in the region of the moving contact line.
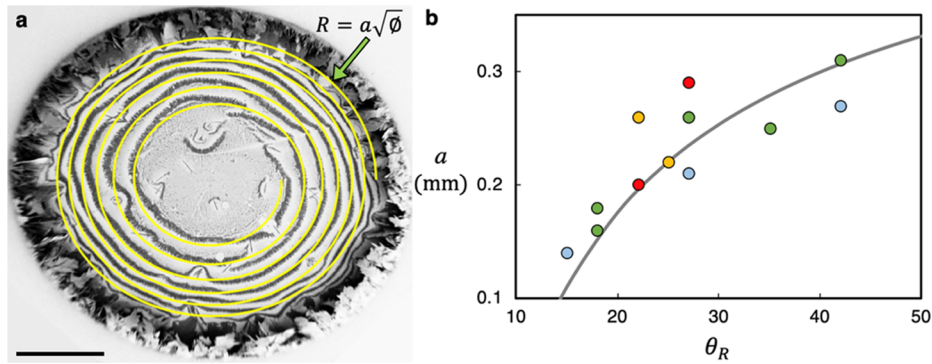

Figure 5. Quantifying spiral shapes. (a) SEM image of a spiral deposit with the relevant solution of Fermat's spiral equation overlaid in yellow, where $a = 0.16$ mm and $\varnothing = [0, 12\pi]$. (b) Proportionality constant a as a function of receding contact angle, where circle markers indicate experimental values (red = 75 °C, orange = 70 °C, green = 65 °C, blue = 60 °C) and the gray line is the model presented in eq 2, with $\theta_{depin} = 10$, $R_o = 1.2$ mm, and $\theta_{pin} = \theta_R$. The scale bar indicates 0.5 mm.

Figure 4a) with a preslip contact angle θ_{depin} and base dimension equal to $(R_o - R(t))$. After slip, the base dimension of the wedge will have changed by a small amount, which will be approximately equal to a, but with a new contact angle equal to θ_{pin}. If we assume negligible mass loss during this motion, then

$$\frac{1}{2}(R_o - R(t))^2 \tan\theta_{depin} \sim \frac{1}{2}(R_o - R(t) - a)^2 \tan\theta_{pin} \tag{1}$$

Applying the low angle approximation and substituting $(R_o - R(t)) \sim R_o/2$, we find that

$$a \approx \frac{R_o}{2}\left[1 - \left(\frac{\theta_{depin}}{\theta_{pin}}\right)^{1/2}\right] \tag{2}$$

where R_o is the radius of the deposit, θ_{depin} is the contact angle immediately prior to depinning from the array of crystalline needles, and θ_{pin} is the contact angle just after repinning. For a drop evaporating in a standard mode (where the contact line motion moves inward), θ_{depin} would be equivalent to the receding contact angle θ_R and θ_{pin} could be estimated as the equilibrium contact angle. Here, the contact line motion of the evaporating thin film deviates strongly from this case. Crystals formed at the pinned contact line are highly wetting, meaning that the depinning contact angle becomes a function of the

crystal wettability rather than of the surface itself. Thus, θ_{depin} will be constant across substrates and have a value smaller than that of the actual receding contact angles. Likewise, θ_{pin} is not equal to the equilibrium contact angle, but is rather much smaller, and is likely even smaller than the substrate's contact angle (see side-view movie included in the SI). However, unlike θ_{depin}, there is a clear dependence of θ_{pin} on the substrate wetting properties. Thus, we approximate θ_{pin} as the receding contact angle for the purposes of plotting eq 2 against experimental data (Figure 5b, with $\theta_{depin} = 10°$, $R_o = 1.2$ mm).

The experimental data presented in Figure 5b include spirals formed at 60 °C (blue), 65 °C (green), 70 °C (orange), and 75 °C (red). The geometric parameter a generally increases with increasing temperature. A temperature correction could easily be incorporated into this model by altering the assumption that mass lost during a stick-slip event is negligible and by adding a loss term on the right-hand side of eq 1. This term would increase the value of a, consistent with the result that a increases with increasing temperatures/evaporation rates. Previous work showing formation of fullerene spirals in conjunction with a glass bead on a hydrophilic surface demonstrated a strong temperature dependence of the winding, in which the distance between pattern arcs increased with temperature.[30] In the present work, the temperature dependence is much less dramatic, which might be attributed to the negligible change of calcium sulfate's solubility with temperature.
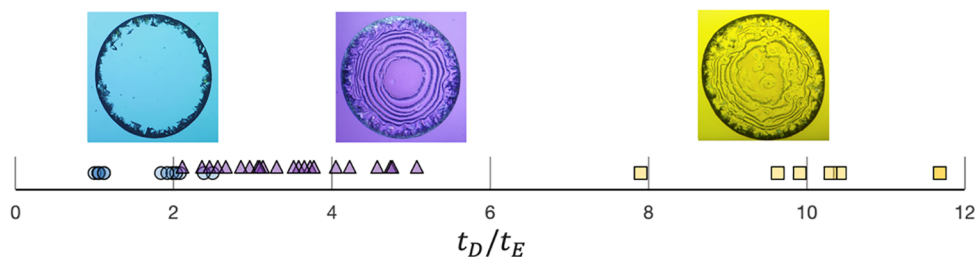
Figure 6. Line plot of eq 7, where rings (blue circles) form at low values, patterns (purple triangles) form in the intermediate region, and random deposition (yellow squares) occurs at higher values. Selected images show examples of the patterns represented.

We have demonstrated that contact line dynamics control both the pattern type (spiral or concentric ring) and the pattern geometry (the distance between subsequent spiral arcs and concentric rings). However, additional dynamics are required to understand the regimes in which patterns form. Regular patterns that mirror the contact line motion on the drop interior only form on substrates heated to temperatures between ca. 60 and 75 °C. Slower evaporation on cooler substrates forms few, or no, crystals on the drop interior, while faster evaporation on hotter substrates forms a more chaotic distribution of crystals. Thus, we consider evaporative dynamics to understand this behavior, starting with the rate of change for the local height of a thin film for a completely wetting, evaporating drop[33]

$$\frac{dh(r,t)}{dt} = -\frac{J_o}{R(t)\sqrt{\frac{r^2}{R(t)^2} - 1}} \tag{3}$$

where J_o is the diffusion-driven evaporative flux in m²/s ($J_o = D_{vap}(C_T - C_{oo})/\rho$, where D_{vap} is the diffusion coefficient of water vapor in air, C_T is the concentration of water vapor at the interface at the substrate temperature T, C_{oo} is the concentration of water vapor in the ambient environment, and ρ is the density of water). In this equation, r is the radial position starting from the drop interior and moving toward the outer crystal ring so that evaporation flux has a minimum at $r = R_o$ and a singularity at the moving contact line where evaporative flux is largest.[34] Equation 3 originates from an electrostatic analogy applied to evaporating drops (see SI, and refs 3 and 30) and reflects the result that maximal evaporative flux occurs at the contact line.[34]

To estimate the timescale of evaporation in the region of the mobile contact line and to avoid the singularity at $r = R(t)$, we use $r = R(t) + \Delta r$, where Δr is some small length scale (see Figure 4c). Substituting this relation into eq 3, dropping the term $\Delta r^2/R(t)^2$ due to its insignificant size, and rearranging as a scaling argument, where $R(t) = R_{pin}$ (where R_{pin} is the radius at which patterning begins), we find

$$\frac{\Delta h}{t_E} \sim \frac{J_o}{\sqrt{\Delta r R_{pin}}} \tag{4}$$

where t_E is the timescale of evaporation at the moving contact line. Rearranging to solve for this timescale, we find

$$t_E = \frac{\Delta h \sqrt{\Delta r R_{pin}}}{J_o} \tag{5}$$

To understand the physics of pattern formation, the evaporative timescale must be compared to a timescale describing the process of crystallization at the mobile contact

line. We observe that rings form at low evaporation rates (Figure 2) while spiral or concentric ring patterns form at higher rates, and amorphous crystals form at the highest evaporation rates. If salt ions are able to move away from the contact line faster than the mobile contact line can "catch" them, crystallization will occur at the already existing outer crystalline ring, resulting in a single ring. If the movement of the salt ions is slow, they will be forced to precipitate as crystals as the contact line moves past them. When the motion of the contact line is too fast, the precipitation occurs randomly, giving rise to the amorphous deposits observed at the very highest temperatures. Calcium ions are smaller and more mobile than sulfate ions, and therefore, we use the diffusivity of calcium ions to capture the timescale of ion motion

$$t_D = \frac{\Delta r^2}{D_{Ca^{2+}}} \tag{6}$$

where $D_{Ca^{2+}}$ is the diffusion coefficient of calcium ions in water. Finally, the ratio of the evaporative timescale of eq 5 and the diffusive scale of eq 6 should allow for dimensionless prediction of pattern formation. This ratio is

$$\frac{t_D}{t_E} = \frac{J_o}{D_{Ca^{2+}}} \frac{\Delta r}{\Delta h} \sqrt{\frac{\Delta r}{R_{pin}}} \tag{7}$$

We assume that Δr is approximately equal to the width of the crystalline rings, as shown in Figure 4c (30 μm), and estimate $\Delta h = \Delta r \tan \theta_{depin} \approx 5$ μm, for $\theta_{depin} = 10°$. The evaporative flux J_o and diffusion $D_{Ca^{2+}}$ are both functions of temperature (see SI), and R_{pin} is taken from experimental data. Finally, we test the hypothesis that this ratio can be used to classify the emergence of patterns by calculating this ratio (eq 7) for each of the examples shown in Figure 2. The results of this analysis are shown in Figure 6, where the blue circles indicate a single, empty ring; purple triangles indicate interior patterning (either concentric ring or spiral); and yellow squares indicate random crystalline deposits at the drop interior. Although both the diffusion rate and evaporation rate increase with temperature, the evaporative flux increases faster, leading to good separation between the different categories.

Based on the results of Figure 6 and eq 7, we find that the two parameters important for patterning are (1) the system geometry and (2) the ratio of evaporation to diffusion. In particular, the ratio of the relative height and radial dimension of the evaporating drop profile will affect whether or not this contact line patterning phenomenon will occur. These dimensions are partially controlled by the height of the outer crystalline ring, which grows during the first stages of evaporation. Without this three-dimensional feature, the interior patterns would fail to form (see the SI for experiments

using salts that do not form the outer ring and do not exhibit contact line motion patterning). However, patterning via this process is not unique to calcium sulfate. Any solute that forms a three-dimensional exterior ring during the early stages of evaporation when evaporated on these high hysteresis surfaces has the potential to form patterns (see SI, where concentric ring deposits of silver sulfate and sodium chloride are shown), so long as both the drop geometry and evaporation-to-diffusion ratios are within the correct regime, as predicted by eq 7. This result also provides an explanation for why the latex beads do not exhibit the same contact line behavior, as the beads also do not form a three-dimensional outer ring.

CONCLUSIONS

Evaporating drops of calcium sulfate on substrates with extreme contact angle hysteresis always leads to the formation of a three-dimensional outer crystalline ring at the drop contact radius. However, relatively flat crystalline patterns may also arise on the interior of this ring depending on the ratio of the evaporation rate and the diffusion rate. Fast evaporation leads to the formation of amorphous, chaotic crystal deposits on the interior, while slower evaporation leads to no crystallization at the interior contact line. At intermediate rates, crystalline patterns in the form of concentric rings or spirals emerge. A simple mass balance argument can be used to calculate the geometry of spiral patterns, where lower substrate receding contact angles result in tighter winding of the patterns.

The prevalence of spirals in biology and nature is due to the principle of parsimony, which states that nature develops in the simplest and most efficient path. This principle can (and should) also be applied to engineering, and spiral shapes are desirable in any application in which "compact length" is desired.[32] Two-dimensional Fermat spirals such as those formed in the present work have a range of applications, including creation of substrates with alternating hydrophobic/hydrophilic regions, templates for spiral microfluidic channels,[35,36] ring resonators for optics (where the low curvature of the Fermat spiral at the center allows for minimal losses),[37] spiral cantilevers for microscale sensors[38] and cochlear implants,[39] spiral antennas,[40,41] and spiral electrodes for harvesting mechanical energy.[42] Aside from being fast and inexpensive, our method for designing spiral templates from evaporating drops is scalable and easy to implement, and therefore has the potential to alter how micro- and millimetric-scale spiral devices are produced.

METHODS

Procedures. Saturated calcium sulfate solution was prepared by adding calcium sulfate dihydrate salt (Sigma-Aldrich) to deionized (DI) water in excess. Calcium sulfate was chosen as a model salt because of its temperature-independent solubility (allowing for the use of temperature to control the evaporation rate) and because it crystallizes readily. The solution was mixed for a period of several days before excess solid was filtered out. Substrates were heated to specified temperatures using a commercial hotplate and thermal paste. Independent temperature measurements were also taken via a thermocouple to ensure that temperature at the substrate surface matched the hotplate set point. Drops (5 μL) of calcium sulfate were gently pipetted onto the surface, and videos were recorded from the top and side. The timescale of transience for drops to reach equilibrium temperature has been previously estimated to be 7 s,[12] which is significantly shorter than the evaporation time even for the largest evaporation rates.

Substrates. Preparation and characterization methods for these surfaces have been reported in previous investigations.[43] In short, surfaces were prepared by sputtering ceria or erbia chemistries onto silicon wafers to depths ranging between 300 and 400 nm. Because sputtered coatings often result in nonequilibrium films and are heavily dependent on the process parameters, these surfaces were relaxed under vacuum for periods of months to years to reach optimal surface stiochiometry.[44] The sputter depth gives rise to the different substrate colors observed throughout the figures and contributes to altered contact angles. The origin of the large contact angle hysteresis of these surfaces is not fully understood, but for the most hydrophobic surface (blue ceria; depth, ~350 nm), it seems to primarily arise from chemical inhomogeneity, while the two surfaces with the lowest receding contact angles exhibit significant roughness, which contributes to pinning. Surface advancing, equilibrium, and receding contact angles were recorded prior to experiments using a goniometer and 5 μL drops of DI water. For additional information on substrate characterization, including layer depth, roughness, and X-ray photoelectron spectroscopy (XPS) images, see the Supporting Information (SI).

Images. Optical top-view images shown in Figures 1−3 and 6 were obtained from videos using a Nikon D300 camera attached to a Zeiss AxioZoom V.16 microscope equipped with a PlanApo ZO 0.5× magnifying lens. Image colors are real and result from different sputter depths of the substrates (see SI). In some images, brightness, contrast, and/or saturation was tuned up or down for consistency across a given substrate, but care was taken to preserve original data. Optical side-view images shown in Figure 1 were recorded as videos using a Nikon D800 camera equipped with a Navitar lens. SEM images of Figures 4c and 5a were obtained using a Zeiss Gemini Supra55VP Field Emission Scanning Electron Microscope. The spiral overlay on Figure 5a was added using MatLab.

ASSOCIATED CONTENT

Ⓢ Supporting Information

The Supporting Information is available free of charge on the ACS Publications website at DOI: 10.1021/acs.langmuir.9b01002.

> Complete evaporation from the side view (MOV)
> Complete evaporation for a concentric ring deposit from the top view (MOV)
> Bursting of a drop creating both spiral and concentric ring morphologies (MOV)
> Timescale data, derivation of the bursting timescale and derivation of eq S3, analysis of pinning/hysteresis forces, details on substrate characterization (contact angles, XPS, roughness, and sputter-coating depth), control experiments using nanoparticles and other salts, data used to generate Figure S4 and an alternative model for how physical principles predict formation of Fermat's spiral in this geometry, and a note on repeatability (PDF)

AUTHOR INFORMATION

Corresponding Author
*E-mail: Varanasi@mit.edu.

ORCID
Samantha A. McBride: 0000-0002-6402-1359
Kripa K. Varanasi: 0000-0002-6846-152X

Author Contributions
The manuscript was written through contributions of all authors. Experiments were designed by S.A.M., S.D., and K.K.V. and conducted by S.A.M. and S.K., and data were analyzed by S.A.M. and K.K.V. All authors have given approval to the final version of the manuscript.

◼ REFERENCES

(1) Ball, P. *Shapes: Nature's Patterns: a Tapestry in Three Parts*; OUP Oxford, 2009.

(2) Assenheimer, M.; Steinberg, V. Transition between spiral and target states in Rayleigh−Bénard convection. *Nature* **1994**, *367*, 345−347.

(3) Deegan, R. D.; et al. Capillary flow as the cause of ring stains from dried liquid drops. *Nature* **1997**, *389*, 827−829.

(4) Shmuylovich, L.; Shen, A. Q.; Stone, H. A. Surface morphology of drying latex films: Multiple ring formation. *Langmuir* **2002**, *18*, 3441−3445.

(5) Yunker, P. J.; Still, T.; Lohr, M. A.; Yodh, A. G. Suppression of the coffee-ring effect by shape-dependent capillary interactions. *Nature* **2011**, *476*, 308−311.

(6) Wong, T.-S.; Chen, T.-H.; Shen, X.; Ho, C.-M. Nano-chromatography Driven by the Coffee Ring Effect. *Anal. Chem.* **2011**, *83*, 1871−1873.

(7) Cui, L.; et al. Avoiding coffee ring structure based on hydrophobic silicon pillar arrays during single-drop evaporation. *Soft Matter* **2012**, *8*, 10448.

(8) Bhardwaj, R.; Fang, X.; Somasundaran, P.; Attinger, D. Self-Assembly of Colloidal Particles from Evaporating Droplets: Role of DLVO Interactions and Proposition of a Phase Diagram. *Langmuir* **2010**, *26*, 7833−7842.

(9) Liu, L.; et al. Regulation of the Deposition Morphology of Inkjet-Printed Crystalline Materials via Polydopamine Functional Coatings for Highly Uniform and Electrically Conductive Patterns. *ACS Appl. Mater. Interfaces* **2016**, *8*, 21750−21761.

(10) Gulka, C. P.; et al. Coffee Rings as Low-Resource Diagnostics: Detection of the Malaria Biomarker Plasmodium falciparum Histidine-Rich Protein-II Using a Surface-Coupled Ring of Ni(II)-NTA Gold-Plated Polystyrene Particles. *ACS Appl. Mater. Interfaces* **2014**, *6*, 6257−6263.

(11) Lin, Z. *Evaporative Self-Assembly of Ordered Complex Structures*; World Scientific, 2012.

(12) McBride, S. A.; Dash, S.; Varanasi, K. K. Evaporative Crystallization in Drops on Superhydrophobic and Liquid-Impregnated Surfaces. *Langmuir* **2018**, *34*, 12350.

(13) Mullin, J. W. *Crystallization*, 4th Edition: Butterworth-Heinemann: Woburn, MA, 2001.

(14) Shahidzadeh-Bonn, N.; Rafai, S.; Bonn, D.; Wegdam, G. Salt Crystallization during Evaporation: Impact of Interfacial Properties. *Langmuir* **2008**, *24*, 8599−8605.

(15) Shahidzadeh, N.; Schut, M. F. L.; Desarnaud, J.; Prat, M.; Bonn, D. Salt stains from evaporating droplets. *Sci. Rep.* **2015**, *5*, No. 10335.

(16) Shin, B.; Moon, M.-W.; Kim, H.-Y. Rings, Igloos, and Pebbles of Salt Formed by Drying Saline Drops. *Langmuir* **2014**, *30*, 12837−12842.

(17) Du, R.; Stone, H. A. Evaporatively controlled growth of salt trees. *Phys. Rev. E* **1996**, *53*, 1994−1997.

(18) Good, R. J. *Contact Angle, Wettability, and Adhesion*; Mittal, K. L., Ed.; VSP: Utrecht, 1993; pp 3−36.

(19) Gao, N.; et al. How drops start sliding over solid surfaces. *Nat. Phys.* **2018**, *14*, 191−196.

(20) de Gennes, P.-G.; Brochard-Wyart, F.; Quéré, D. *Capillarity and Wetting Phenomena: Drops, Bubbles, Pearls, Waves*; Springer, 2004.

(21) McHale, G.; Erbil, H. Y.; Newton, M. I.; Natterer, S. Analysis of shape distortions in sessile drops. *Langmuir* **2001**, *17*, 6995−6998.

(22) Baldwin, K. A.; Fairhurst, D. J. Classifying dynamic contact line modes in drying drops. *Soft Matter* **2015**, *11*, 1628−1633.

(23) Deegan, R. D. Pattern formation in drying drops. *Phys. Rev. E* **2000**, *61*, 475−485.

(24) Li, W.; Lan, D.; Wang, Y. Dewetting-mediated pattern formation inside the coffee ring. *Phys. Rev. E* **2017**, *95*, 042607.

(25) Keller, J. B. Breaking of liquid films and threads. *Phys. Fluids* **1983**, *26*, 3451−1128.

(26) Shanahan, M. E. R. Simple Theory of Stick-Slip and Wetting Hysteresis. *Langmuir* **1995**, *11*, 1041−1043.

(27) Shanahan, M. E. R.; Sefiane, K. *Contact Angle, Wettability, and Adhesion*; Mittal, K. L., Ed.; CRC Press, 2009; Vol. 6, pp 19−31.

(28) Wu, M.; Man, X.; Doi, M. Multi-ring Deposition Pattern of Drying Droplets. *Langmuir* **2018**, *34*, 9572.

(29) Mae, K.; et al. Self-Organized Micro-Spiral of Single-Walled Carbon Nanotubes. *Sci. Rep.* **2017**, *7*, No. 5267.

(30) Chen, Y.-J.; Suzuki, K.; Yoshikawa, K. Self-organized target and spiral patterns through the "coffee ring" effect. *J. Chem. Phys.* **2015**, *143*, No. 084702.

(31) Chen, Y.-J.; Suzuki, K.; Mahara, H.; Yoshikawa, K.; Yamaguchi, T. Self-organized Archimedean spiral pattern: Regular bundling of fullerene through solvent evaporation. *Appl. Phys. Lett.* **2013**, *102*, No. 041911.

(32) Pickover, C. A. Mathematics and Beauty: A Sampling of Spirals and 'Strange' Spirals in Science, Nature, and Art. *Leonardo* **1988**, *21*, 173−181.

(33) Cachile, M.; Bénichou, O.; Cazabat, A. M. Evaporating Droplets of Completely Wetting Liquids. *Langmuir* **2002**, *18*, 7985−7990.

(34) Hu, H.; Larson, R. G. Evaporation of a Sessile Droplet on a Substrate. *J. Phys. Chem. B* **2002**, *106*, 1334.

(35) Nie, Y.; Hao, N.; Zhang, J. X. J. Ultrafast Synthesis of Multifunctional Submicrometer Hollow Silica Spheres in Microfluidic Spiral Channels. *Sci. Rep.* **2017**, *7*, No. 12616.

(36) Warkiani, M. E.; Tay, A. K. P.; Guan, G.; Han, J. Membrane-less microfiltration using inertial microfluidics. *Sci. Rep.* **2015**, *5*, No. 11018.

(37) Xu, D.-X.; et al. Archimedean spiral cavity ring resonators in silicon as ultra-compact optical comb filters. *Opt. Express* **2010**, *18*, 1937.

(38) Wilson, S. A.; et al. New materials for micro-scale sensors and actuators: An engineering review. *Mater. Sci. Eng., R* **2007**, *56*, 1−129.

(39) Udvardi, P.; et al. Spiral-Shaped Piezoelectric MEMS Cantilever Array for Fully Implantable Hearing Systems. *Micromachines* **2017**, *8*, 311.

(40) Mao, L.; et al. Far-field radially polarized focal spot from plasmonic spiral structure combined with central aperture antenna. *Sci. Rep.* **2016**, *6*, No. 23751.

(41) Wen, H.; Yang, J.; Zhang, W.; Zhang, J. Optical resonant Archimedean spiral antennas. *J. Nanophotonics* **2011**, *5*, No. 053523.

(42) Chen, L.; et al. Novel Spiral-Like Electrode Structure Design for Realization of Two Modes of Energy Harvesting. *ACS Appl. Mater. Interfaces* **2015**, *7*, 16450−16457.

(43) Azimi, G.; Dhiman, R.; Kwon, H.-M.; Paxson, A. T.; Varanasi, K. K. Hydrophobicity of rare-earth oxide ceramics. *Nat. Mater.* **2013**, *12*, 315−320.

(44) Chin, C. C.; et al. On the off stoichiometry of cerium oxide thin films deposited by RF sputtering. *Phys. C* **1996**, *260*, 86−92.